

# Chapitre 9

## Le cas du vent à deux composantes

### 9.1 Motivations et plan

Devant la difficulté de reproduire la diversité des profils de raies des quasars de type BAL à l'aide du simple modèle en expansion sphérique (p.ex. Weymann & Foltz [1983], Turnshek et al. [1988], Korista et al. [1993]), nous avons décidé de modifier le programme MCRT afin de pouvoir considérer d'autres types de géométries de vents. Une géométrie un peu plus complexe à laquelle on peut penser est la symétrie cylindrique dans laquelle on introduit la présence d'une composante équatoriale. Ce type de symétrie n'est pas nécessairement singulière en astrophysique. En effet ce type de modèle a déjà fait l'objet d'investigations pour expliquer les profils de raies issus des vents d'étoiles massives de type Be (Bjorkman et al. [1994]) où encore dans le cas des profils de raies produits par un disque d'accrétion (e.a. Knigge et al. [1995]). Ce type de géométrie est également suggérée afin de rendre compte des propriétés spectropolarimétriques des quasars BAL (e.a. Ogle et al. [1999], Lamy & Hutsemékers [2004]).

Après avoir présenté les détails du modèle de vent à deux composantes et discuté une méthode de diminution du temps de calcul dans le cas d'un vent ne présentant plus de symétrie sphérique, nous comparerons qualitativement les spectres obtenus à l'aide de MCRT et ceux produits par une adaptation de la méthode SEI au cas des vents axisymétriques (Bjorkman et al. [1994]). La dernière section de ce chapitre sera consacrée à l'article soumis pour publication à la revue *Astronomy & Astrophysics*, montrant que le modèle de vent discuté ici permet de reproduire la plupart des profils de la raie du CIV observés dans un échantillon de quasars BAL. Cet article présente également de

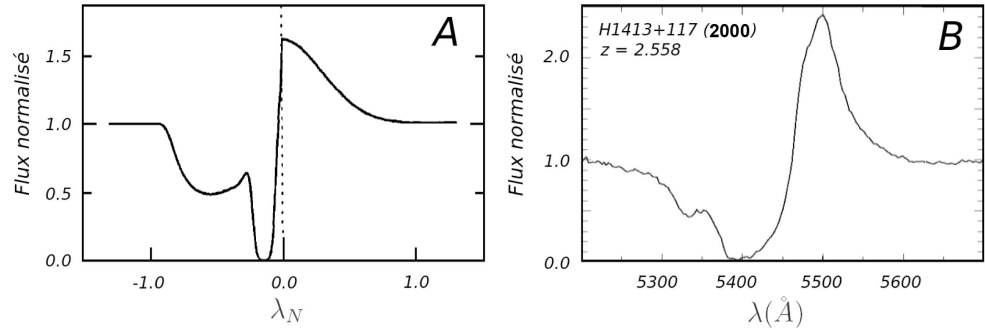


FIG. 9.1 – Comparaison d'un profil de raie de résonance simulé dans un vent à deux composante (extraite de Bjorkman et al. [1994]) et du profil de raie de l'ion CIV du quasar H1413+117. Etant donné la ressemblance entre les deux spectres, il est facile de se convaincre qu'un vent à deux composantes permet d'expliquer, du moins qualitativement, les profils de raies produits dans les quasars de type BAL, ainsi que l'existence d'une composante étroite et profonde en absorption du côté bleu de la raie.

façon succincte l'effet des différents paramètres du vent à deux composantes sur les profils simulés.

## 9.2 Loi de vitesse et de densité utilisées

Nous avons modifié le code MCRT de façon à pouvoir considérer la présence à la fois d'un vent en expansion sphérique et d'un vent de type équatorial mais aussi d'une possible rotation de l'enveloppe. Etant donné l'allure générale des profils présentés par Bjorkmann et al. [1994] dans le cadre de l'étude des raies de résonances UV présentes dans le spectre de l'étoile HD93521, nous avons décidé d'implémenter le modèle du “wind compressed disk” proposé par Bjorkman & Cassinelli [1993]. En pratique, nous considérons maintenant l'existence d'un champ de vitesse de type :

$$\vec{v} = v_r(r, \theta) \vec{e}_r + v_\phi(r, \theta) \vec{e}_\phi + v_\theta(r, \theta) \vec{e}_\theta \quad (9.1)$$

pour lequel nous supposons, comme Bjorkman et al. [1994], que la composante de vitesse selon la direction  $\vec{e}_\theta$  est de valeur nulle. La composante  $v_r$  décrivant l'évolution radiale de la vitesse est la loi typique en  $\beta$  utilisée dans la section précédente :

$$v_r(r, \theta) = v_{min} + (v_{max}(\theta) - v_{min}) \left(1 - \frac{R_{in}}{r}\right)^\beta. \quad (9.2)$$

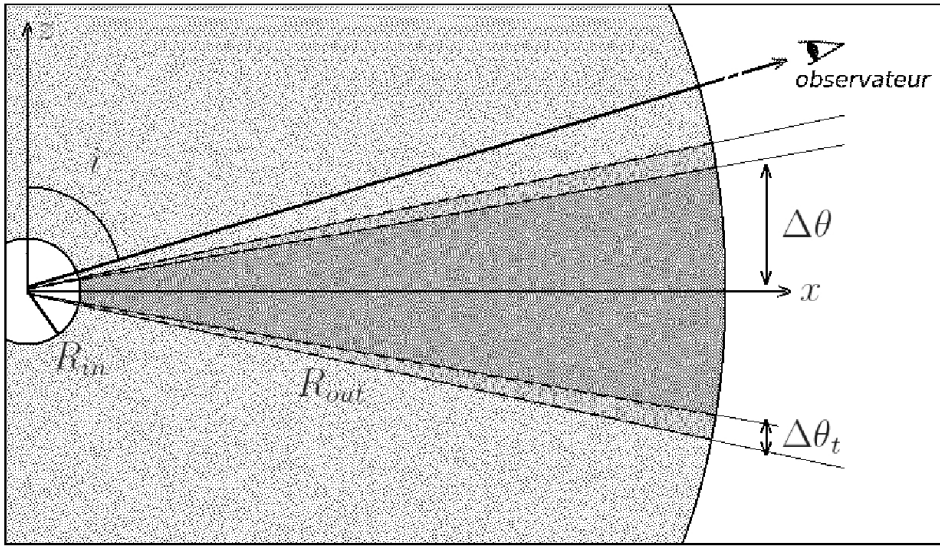


FIG. 9.2 – Illustration dans le plan  $(x,z)$  du modèle de vent à deux composantes utilisée (cf. Bjorkmann et al. [1994])). L'ouverture totale du vent équatorial est de  $2\Delta\theta$ . L'épaisseur angulaire de la zone de transition entre le vent polaire et le vent équatorial est fixée par le paramètre  $\Delta\theta_t$ , et l'observateur à l'infini observe le vent selon un angle d'inclinaison  $i$  défini par rapport à l'axe du vent équatorial.

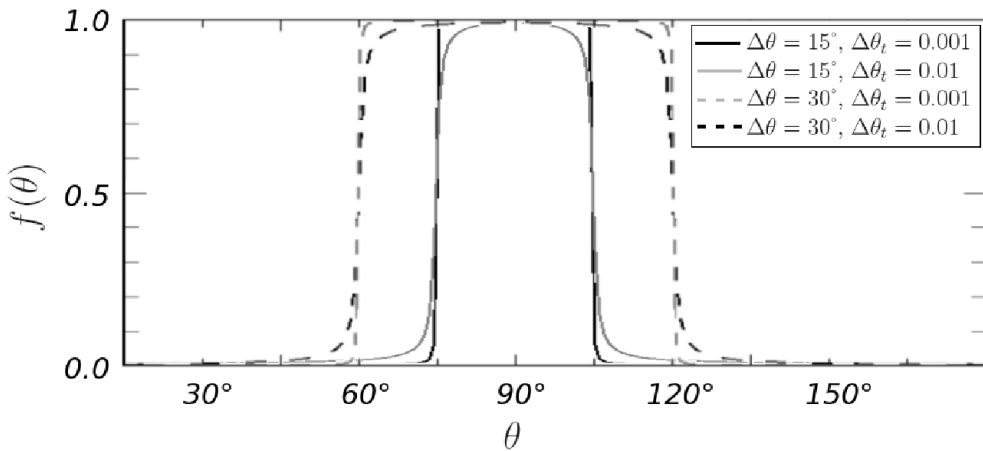


FIG. 9.3 – Illustration de la loi  $f(\theta)$  (cf. Eq. (9.4)) gouvernant la transition entre les composantes polaire et équatoriale du vent pour deux valeurs des paramètres  $\Delta\theta$  et  $\Delta\theta_t$ . En pratique nous utilisons toujours une zone de transition très fine par rapport au disque (i.e.  $\Delta\theta_t = 0.001$ ).

Afin d'introduire une composante équatoriale au vent, on définit une vitesse terminale  $v_{max}(\theta)$  dépendant de la latitude  $\theta$  :

$$v_{max}(\theta) = v_{max}^{po} + (v_{max}^{eq} - v_{max}^{po})f(\theta) \quad (9.3)$$

où  $v_{max}^{po}$  et  $v_{max}^{eq}$  sont respectivement les vitesses terminales des composantes polaire et équatoriale du vent et où la fonction  $f(\theta)$  contrôle la transition (Fig. 9.3) entre les deux composantes :

$$f(\theta) = \frac{1}{2} \left( 1 + \frac{2}{\pi} \operatorname{atan} \left( \frac{\sin \Delta\theta - \cos \theta}{\Delta\theta_t} \right) \right). \quad (9.4)$$

ici  $2 \Delta\theta$  représente l'ouverture angulaire du disque équatorial et  $\Delta\theta_t$  contrôle l'épaisseur de la région de transition entre le vent polaire et le vent équatorial (Fig. 9.2). La composante  $v_\phi$  vérifie la relation de conservation du moment angulaire et s'écrit :

$$v_\phi = V_{rot} \sin \theta \left( \frac{R_{in}}{r} \right) \quad (9.5)$$

où  $V_{rot}$  est la vitesse de rotation à la base du vent équatorial en  $\theta = 90^\circ$ .

Pour la loi de densité d'ions dans le vent, nous utilisons une loi semblable à celle définie dans la section précédente :

$$n(r) = n_0(\theta) \left( \frac{r}{R_{in}} \right)^{-\alpha} \left( \frac{v_r(r, \theta)}{v_{min}} \right)^{-1} \quad (9.6)$$

mais où la densité initiale en  $r = R_{in}$  varie en fonction de la latitude  $\theta$  :

$$n_0(\theta) = n_0^{po} + (n_0^{eq} - n_0^{po})f(\theta) \quad (9.7)$$

où  $n_0^{po}$  et  $n_0^{eq}$  sont respectivement les densités initiales dans les régions polaire et équatoriale et où  $f(\theta)$  a été défini par l'Eq. (9.4). Comme dans le cas du vent en expansion sphérique, la valeur de  $n_0^{po}$  est déterminée en imposant la valeur  $\tau_{tot_E}$  de l'opacité polaire totale (i.e. en  $\theta = 0^\circ$ ). La densité initiale de la composante équatoriale est fixée par la relation  $n_0^{eq} = k_{pm}n_0^{po}$ ,  $k_{pm}$  étant le rapport de densité de la composante équatoriale par rapport à la composante polaire.

### 9.2.1 La production de spectres et d'images dans la cas d'un vent à deux composantes

Dans la Sect. A.2.4 nous avons montré comment MCRT pouvait produire des images  $I(x, y, \nu)$  fournissant la distribution de brillance du vent pour

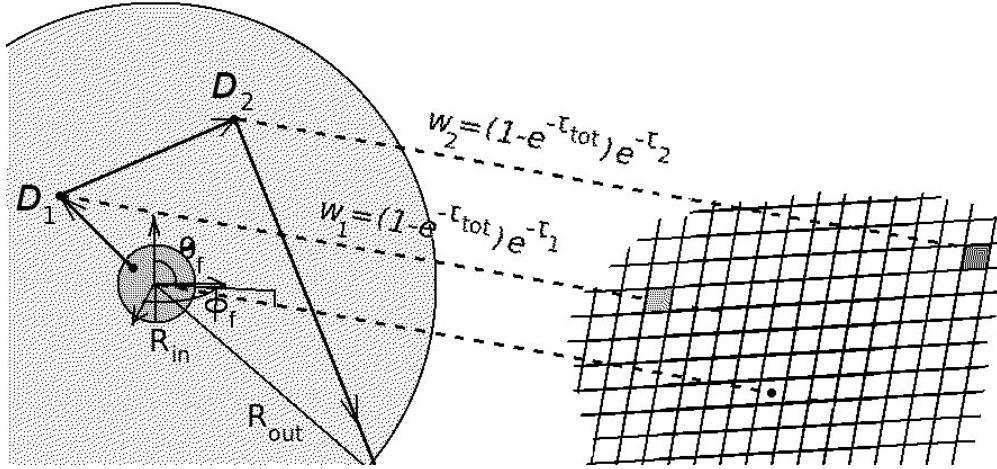


FIG. 9.4 – Illustration du “Peeling off” du paquet de photon dans le cas où ce dernier subirait deux diffusions dans le vent  $D_1$  et  $D_2$ . Pour chaque interaction  $D_i$  nous estimons la fraction  $w_i$  du paquet de photon parvenant à s'échapper de l'atmosphère en direction du détecteur (représenté ici par un capteur CCD).

chaque tranche de fréquence  $\nu \pm d\nu/2$  du spectre simulé pour une direction d'observation donnée ( $d\nu$  étant l'élément de résolution spectrale choisi pour le spectre). Nous avons également discuté la simplification existante lorsque le modèle de vent considéré possède une symétrie sphérique. Ici, l'introduction d'une composante équatoriale dans le vent entraîne une perte de symétrie en latitude du vent : la probabilité de fuite des photons est maintenant fonction non seulement de leur fréquence  $\nu$  mais également de l'angle d'observation considéré. Nous ne pouvons dès lors plus créer les spectres et les images en groupant simplement selon leur fréquence finale tous les photons s'échappant du modèle : il faut également tenir compte de leur direction de sortie. Ainsi lors des simulations réalisées, seule une petite partie des photons parviendront à s'échapper selon la direction d'observation choisie, produisant des spectres et des images de faible  $S/N$  malgré un nombre de photons utilisés extrêmement grand.

Afin de pallier à ce problème, nous avons implémenté une routine de “Peeling off” (e.a. Yusef-Zadeh et al. [1984], Wood & Reynolds [1999]) dans le programme MCRT. L'idée à la base de cette méthode est la suivante : à chaque interaction d'un photon avec le vent, une partie du paquet de photons sera forcée à se diriger vers l'observateur. Considérons un paquet de photons de fréquence  $\nu$  et de direction de vol  $\vec{n}_v$  pour lequel une ou plusieurs zones de résonances ont été repérées le long de sa trajectoire dans le vent. On peut alors calculer l'opacité totale  $\tau_{tot}$  que ce paquet va rencontrer le long de son

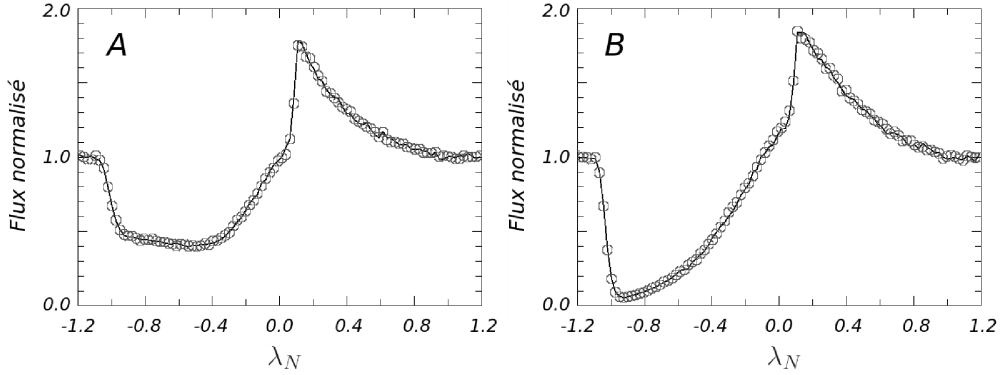


FIG. 9.5 – Illustration de l'équivalence des spectres produits en considérant le “Peeling off” (cercles gris) du paquet de photon pour un observateur situé selon la direction  $(\theta_o, \phi_o) = (45^\circ, 90^\circ)$  ou non (MCRT “traditionnel”, en trait continu) pour une atmosphère en expansion sphérique de paramètres choisis. Deux cas d'épaisseur optique totale différente sont représentés.

voyage et le forcer à interagir en un point  $\vec{r}_1$  tel que  $\tau_{\vec{r}_1} < \tau_{tot}$  si l'on corrige le biais introduit par cette interaction forcée (cf. Sect. A.3.1). En ce point  $\vec{r}_1$  nous pouvons calculer la profondeur optique  $\tau_1$  traversée par le paquet de photon dans le cas où ce dernier serait réémis en direction de l'observateur. La fraction du paquet de photon pouvant alors atteindre l'observateur selon cette direction est donnée par :

$$w_1 = (1 - e^{-\tau_{tot}}) e^{-\tau_1} HG(\theta) \quad (9.8)$$

où  $HG(\theta) = 1/(4\pi)$  dans le cas d'une émission isotrope. Cette fraction  $w_1$  est enregistrée par les différents détecteurs afin de produire les spectres et images de la simulation. Le reste du paquet de photon poursuit quant à lui son chemin dans le vent en étant réémis dans une direction aléatoire. Si ce paquet interagit en un autre point  $\vec{r}_2$  de sa trajectoire, nous pouvons de même calculer l'épaisseur optique  $\tau_2$  que le photon devrait traverser s'il était réémis en direction de l'observateur et dès lors enregistrer la fraction du paquet de photon atteignant le détecteur :

$$w_2 = (1 - e^{-\tau_{tot}}) e^{-\tau_2} HG(\theta) \quad (9.9)$$

et ainsi de suite pour les éventuelles interactions suivantes (cf. Fig. 9.4).

En pratique, la simulation d'un spectre par cette technique se déroule en deux temps distincts. Dans un premier temps, on réalise ce que l'on appelle la boucle des photons “Peeled off” dans laquelle les paquets de photons sont émis par le continuum dans une direction quelconque. A chaque interaction

$I_i$  de ces derniers avec le vent, on calcule la fraction  $w_i$  du paquet de photon pouvant être détectée selon une direction d'observation choisie. Cette boucle permet de produire la partie en émission du spectre. Afin de simuler la partie en absorption de ce dernier, on réalise dans un second temps ce que l'on appelle la boucle des photons "directs". Pour cela, on force les photons émis par le continuum à se diriger vers l'observateur. Ainsi seules les position d'émission et fréquence sont choisies de façon aléatoire, la direction d'émission étant définie à l'avance. Pour chacun des paquets de photons ainsi émis, on calcule la profondeur optique jusqu'à l'observateur  $\tau_{obs}$  et l'on enregistre le poid  $w_{obs}$  du paquet de photon parvenant à s'échapper de l'enveloppe et arrivant au détecteur :

$$w_{obs} = e^{-\tau_{obs}} HG(\theta) \quad (9.10)$$

où cette fois-ci  $HG(\theta) = 1/2\pi$  étant donné que les photons émis par le continuum sont forcés à s'en écarter (émission sur une demi sphère, cf. Sect. A.2.1).

En guise de test, nous comparons dans la Fig. 9.5 le spectre produit par la méthode MCRT classique à celui produit par la méthode faisant usage du "Peeling off" dans le cas d'un vent en expansion sphérique. Le choix de ce type de vent pour le test vient du fait qu'étant donné sa symétrie sphérique, le spectre observé doit être identique quelque soit la direction d'observation, ce qui nous évite de devoir échantillonner les spectres selon l'angle  $\theta$  afin d'effectuer la comparaison. Nous notons un accord parfait entre les spectres simulés en utilisant ou non le principe du "Peeling off" du paquet de photons. Attirons finalement l'attention sur l'intérêt d'utiliser cette technique afin de produire simultanément des profils de raies pour plusieurs directions d'observation. En effet, la majeure partie du temps nécessaire à la réalisation d'une simulation de Monte-Carlo provient de l'étape concernant la définition de la trajectoire empruntée par le photon suivi (i.e. repérage des zones de résonances et recherche du point d'interaction). Une fois la position d'interaction selon une direction de vol donnée repérée, il revient pratiquement au même de réaliser le "peeling off" du paquet de photon selon une direction ou selon plusieurs directions. L'utilisation de cette technique particulière s'avère donc avantageuse lors de la réalisation d'atlas de profils pour lesquels des profils de raies d'un même vent sont calculées pour plusieurs directions d'observations. De même le gain en temps est considérable<sup>1</sup> lors du calcul d'un spectre pour un angle d'observation choisi étant donné qu'ici, tous les photons simulés participent à la production du spectre et des images, et cela

---

<sup>1</sup>Ce gain en temps de simultaion dépend également de l'angle d'observation, étant donné l'existence de régions optiquement plus épaisses à la radiation selon la ligne de visée, et donc desquelles moins de photons nous parviennent au cours d'une simulation traditionnelle.

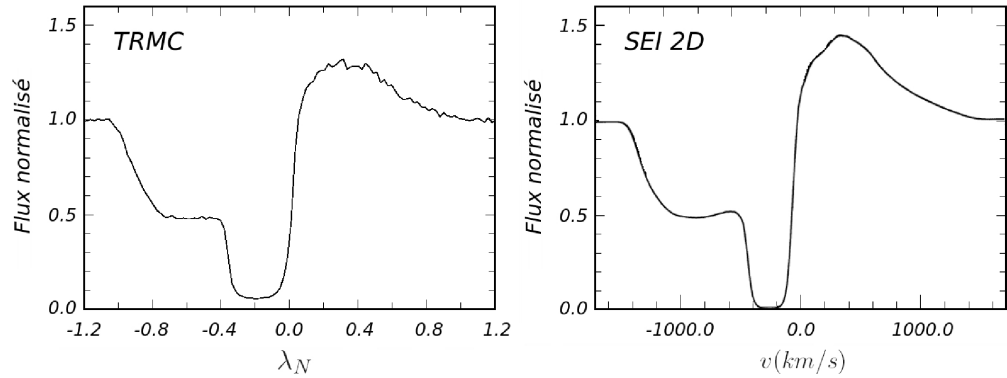


FIG. 9.6 – Illustration de la ressemblance des spectres produits par la méthode MCRT et la méthode SEI adaptée à un vent à deux composantes (Bjorkman et al. [1994]). Les paramètres du vent utilisés ici sont ceux du spectre de référence de la Fig. 10 de Bjorkman et al. [1994], reprise telle quelle dans la partie droite de la figure.

plusieurs fois si ce dernier subit des interactions multiples.

### 9.2.2 Comparaison avec la méthode SEI

La modélisation de raies de résonances dans ce type de vent axisymétrique été implémentée par Bjorkman et al. [1994] en faisant appel à la méthode SEI (cf. Sect. 8.4.3), que ces derniers ont modifiée. L'article décrivant en détail leur implémentation de la méthode SEI dans le cas d'un vent à deux composantes n'est jamais paru dans la littérature (contrairement à ce qui était annoncé par l'auteur dans Bjorkman et al. [1994]). De plus ces derniers indiquent clairement qu'ils ne tiennent pas compte des couplages radiatifs existant entre des points distants de l'enveloppe lors du calcul de la fonction source, une approximation qui n'est plus nécessairement valable lorsque l'enveloppe est optiquement épaisse à la radiation (Mazzali [1990], Petrenz & Puls [1996]).

Nous présentons dans la Fig. 9.6 une comparaison de profil de raie obtenu dans le cas d'un vent à deux composantes pour lequel les paramètres utilisés sont ceux du profil de référence de la Fig. 10 publiée dans Bjorkman et al. [1994] (et reprise ici telle quelle dans le panel de droite). Nous constatons un bon accord général entre les profils obtenus à l'aide de MCRT et de la méthode SEI à deux dimensions. Les légères différences visibles (l'intensité de la composante en émission, la profondeur de la composante étroite en absorption) sont essentiellement dues aux différences entre les lois de densité

utilisées (l'article détaillant leur méthode de calcul n'ayant jamais été publiée, nous avons considéré la loi de densité présentée par l'Eq. (9.6)).

Nous utiliserons par la suite la méthode MCRT, cette dernière tenant explicitement compte des couplages radiatifs, nous permettant ainsi de considérer le cas de vents optiquement épais. De plus, la constitution de MCRT nous permet également de considérer d'autres types de géométries de vents tout en ne nécessitant pas de modification lourde du code sous-jacent.

## 9.3 Modélisation de la raie CIV de quasars BAL à l'aide de la méthode MCRT

### 9.3.1 Résumé de l'article

Malgré de nombreuses études, la géométrie de la région à l'origine des raies d'absorption larges (BAL) observées dans le spectre de près de 20% des quasars reste une question ouverte. Alors que les modèles populaires considèrent une géométrie de type équatoriale pour la région BAL (e.a. Murray et al. [1995]), de récentes observations dans le domaine radio et en spectro-polarimétrie semblent suggérer l'existence d'une population de quasars BAL dont les raies en absorption seraient issues d'un vent polaire (e.a. Becker et al. [2000], Brotherton et al. [2006], Zhou et al. [2006]).

Dans cet article, nous évaluons dans quelle mesure un modèle de vent à deux composantes de type polaire+équatorial est à même de reproduire les profils de raies de résonance du CIV observés dans un échantillon de quasars BAL. Dans ce but, nous avons construit un programme de transfert radiatif original utilisant la méthode de Monte Carlo, MCRT, afin de simuler les profils de raie produits dans un vent possédant ce type de géométrie et d'identifier les paramètres clés gouvernant les profils observés.

Le modèle de vent considéré reproduit efficacement les profils de raies de résonance typiques observés dans les quasars de type BAL, qu'ils soient de type P Cygni ou présentent une forme plus complexe. Les ajustements réalisés suggèrent l'existence d'une composante en rotation rapide autour de l'axe polaire dans les quasars BAL ne présentant pas de profils de raie de type P Cygni. L'angle de vue  $i$  est généralement proche de  $90^\circ$  correspondant à un disque vu par la tranche. Dans certains cas, nous montrons l'existence d'une dégénérescence entre les modèles de vents, certains profils pouvant être tout aussi bien reproduits en considérant des lignes de visées polaires ( $i \sim 0^\circ$ ) ou équatoriales ( $i \sim 90^\circ$ ). Ainsi plusieurs modèles de vents peuvent reproduire les profils de raies observés de sorte que l'ajustement de profils de raies ne suffit généralement pas pour contraindre univoquement les paramètres du vent.

Nous joignons ci-après l'article<sup>2</sup> soumis pour publication à la revue *Astronomy and Astrophysics* détaillant les ajustements réalisés et discutant les résultats obtenus.

---

<sup>2</sup>La référence complète : Borguet, B., Hutsemékers, D. [2009], “A polar+equatorial wind model for Broad Absorption Line quasars : 1. Fitting the CIV BAL profiles” soumis pour publication au journal *A&A*.

# A polar+equatorial wind model for Broad Absorption Line quasars: I. Fitting the C IV BAL profiles

B. Borguet<sup>1,★</sup> and D. Hutsemékers<sup>1,★★</sup>

Institut d'Astrophysique et de Géophysique, University of Liège, Allée du 6 Août 17, B-4000 Liège  
e-mail: b.borguet@ulg.ac.be

Received; accepted

## ABSTRACT

*Context.* Despite a number of study, the geometry at the origin of the blueshifted broad absorption lines (BAL) observed in nearly 20% of quasars still remains a matter of debate.

*Aims.* We want to see if a two component polar+equatorial wind geometry can reproduce typical BAL profiles observed in such objects.

*Methods.* We have build a Monte Carlo Radiative Transfer code (called MCRT) in order to simulate line profiles in such a wind geometry and to identify the parameters governing the line profiles.

*Results.* The two-component wind model appears to be efficient in reproducing typical BAL quasar spectra, from the P Cygni-like line profiles to the more complex profiles. Those fits provide evidence for a high velocity rotation of the wind around the polar axis in BAL quasars with non P Cygni-like line profiles.

**Key words.** Quasars: absorption lines – radiative transfer – Methods: numerical

## 1. Introduction

Depending on the selection technique and the definition used, about 20% to 30% of the quasars detected in recent surveys show in their rest frame UV spectrum the presence of broad absorption line (BAL) troughs associated with the emission lines (e.g. Knigge et al. 2008, Ganguly et al. 2008). These BALs, reminiscent of the P Cygni-type profiles seen in the spectra of massive stars, are mainly observed in high ionization lines like C IV and Si IV and sometimes detected in lower ionization species like Mg II. They reveal strong outflows from quasars (Scargle 1972), which can reach velocities up to 0.2 c (Foltz et al. 1983).

Despite a large number of observations, the physical and geometrical properties of the wind at the origin of the BALs remain largely unknown (e.g. Brotherton 2007). Moreover, the distance at which those objects are found ( $z \geq 1.5$  so that C IV is shifted in the optical domain) hampers the direct observation of the regions at the origin of the BALs even with the best telescopes presently available. Thus, all the information we can get about the inner regions of BAL quasars mainly comes from indirect observations.

The first attempts to model the BAL profiles considered the resonant scattering of photons emitted by a continuum source in a spherically symmetric stellar-like wind (e.g. Scargle et al. 1972). However the growing number of observed spectra displaying a huge variety of line profiles (Korista et al. 1993) revealed the need for other wind models. Facing the diversity of line profiles, Turnshek (1984a) proposed that BAL quasars could be broadly divided into two samples: those quasars which exhibit smooth P Cygni-like profiles, and other ones which display an absorption trough detached in velocity with respect to

the associated weaker and wider emission peak. These observations indicate that the kinematic properties of the wind are more complex than the simple radial outflow inferred for stellar winds (Lee & Blandford 1997). However, as emphasized by Turnshek (1984b), it is very likely that distinct types of BAL QSOs do not exist but are different manifestations of the same phenomenon.

The similarities of the emission line, optical continuum and infrared properties of BAL and non-BAL QSOs (e.g. Weymann et al. 1991, Gallagher et al. 1999, Reichard et al. 2003, Gallagher et al. 2007) as well as the spectropolarimetric observations (e.g. Schmidt & Hines 1999, Ogle et al. 1999, Lamy & Hutsemékers 2004) favored a unification by orientation scheme for the BAL QSOs over the evolutionary scheme (Hazard et al. 1984, Becker et al. 2000). In the unification by orientation scheme, only a fraction (roughly corresponding to the observed fraction of BAL QSOs) of the continuum source is covered by optically thick material producing the broad absorption lines, which suggests a disk-like equatorial geometry for the BAL region (e.g. Turnshek 1984a, Hamann et al. 1993, Murray et al. 1995, Elvis et al. 2000, Yamamoto 2002). Such a geometry is supported by theoretical studies and commonly accepted since the QSOs are thought to be powered by accretion of matter onto a supermassive black hole in the form of a disk, from which the wind could be launched. However, the recent discovery of Radio Loud BAL QSOs (e.g. Becker et al. 2000) and subsequent radio variability studies reveal the existence of polar outflows in at least some of them (Brotherton et al. 2006, Zhou et al. 2006, Ghosh & Punsly 2007). Models combining polar and equatorial components have also been suggested (e.g. Lamy & Hutsemékers 2004) and evaluated from a theoretical point of view (Pereyra et al. 2004, Proga 2003, Proga & Kallman 2004).

In this context and given the similarities between typical BAL profiles (e.g. Korista et al. 1993) and the line profiles produced by a two component polar+equatorial wind like the one

\* PhD. grant student of the Belgian National Fund for Scientific Research (F.N.R.S.)

\*\* Senior research associate F.N.R.S.

presented by Bjorkman et al. (1994), our goal in this first paper is to determine if such a simple two-component wind can qualitatively reproduce the various types of line profiles observed among the BAL QSOs. We will also try to identify the key ingredients needed to reproduce BAL profiles. In a second paper, we will investigate the effect of microlensing on these profiles, aiming at a realistic interpretation of the spectral differences observed in gravitationally lensed BAL QSOs like H1413+117 (cf. Hutsemékers et al. 2009).

In Sect.2, we present MCRT, the Monte Carlo Radiative Transfer code we implemented in order to simulate resonance line profiles in a two-component axisymmetric wind. In Sect.3 we briefly identify the influence of the wind model parameters on the line profiles computed. In Sect.4, we show how MCRT is able to reproduce typical C IV BAL QSOs line profiles. We discuss the results of the line profile fitting and summarize our conclusions in the last two sections of the paper.

## 2. The MCRT code

MCRT is a Fortran77 fully 3D Monte Carlo (MC) Radiative Transfer (RT) code we build up in order to compute resonance line profiles produced in axisymmetric winds. The use of the Monte Carlo simulation technique allows to solve exactly the radiative transfer equation (i.e. without making use of the Sobolev approximation) as well as to ensure for the self consistent treatment of the radiative coupling between distant regions in a wind subject to more complex velocity fields than monotonic radial laws (e.g. Knigge et al. 1995).

Monte Carlo RT code have been extensively described in the literature (e.g. Knigge et al. 1995, Wood et al. 2001, Dijkstra et al. 2006) so that we only remind here the fundamental principles of this technique and the particularities of the MCRT code.

A stated in the introduction, our main goal is the identification of the key ingredients (geometry and overall kinematics) of the wind governing the general profile of the BAL QSO UV resonance lines. Thus we will not consider negligible effects such as the relativistic ones which remain small even for outflows with high ( $v_{\max} \leq 0.2c$ ) terminal speed (Hutsemékers & Surdej 1990), or the fact that the line is a resonance doublet, the velocity separation of the doublet components being small with respect to  $v_{\max}$  (e.g. Hewitt et al. 1974, Grinin 1984).

### 2.1. Radiative Transfer with Monte Carlo techniques

When using the MC technique, the solution of the RT equation is found by following a huge number of photons on their way through the wind. Each step in the photon's life (position and direction of emission, position of interaction, etc) is determined by the mean of random numbers distributed according to the normalized probability density function (NPDF) of the corresponding simulated physical process. Thus if one wishes that the frequency  $\nu_i$  of all of the emitted photons follows a given law  $L(\nu)$  over the frequency interval  $[\nu_{\min}, \nu_{\max}]$ , then  $\nu_i$  will be randomly chosen by solving the transformation equation (Press et al. 1992):

$$\xi = \int_{\nu_{\min}}^{\nu_i} L(\nu) d\nu, \quad (1)$$

where  $\xi$  is a random number drawn from a uniform distribution in the interval  $[0, 1]$ . IN MCRT this number is generated using the “ran2” subroutine of Press et al. (1992). In the following,

each new occurrence of  $\xi$  will refer to the call of such a new random number. In general there is seldom an analytical solution to Eq.1 so we implemented the “table lookup method” (see Avery & House 1968) which allows the use of arbitrary NPDF's.

In MCRT the initial position of emission of the photons is chosen isotropically on the surface of the continuum emission region which is modelled by a sphere of radius  $R_{in}$  and of infinite optical depth ( $\tau_C = \infty$ ) located at the center of the wind. The direction of travel through the wind is then determined by randomly sampling a half sphere taking into account that the photons are forced to leave the continuum source upward.

### 2.2. Continuum photons and resonance scattering

The wind is filled with 2-level atoms whose rest frame normalized absorption profile  $\phi_{abs}$  is described by a gaussian (Natta & Beckwith 1986, Knigge et al. 1995) such that:

$$\phi_{abs}(\nu - \nu_0) = \begin{cases} \phi_{abs}(\nu - \nu_0, \sigma_{turb}) & \text{if } |\nu - \nu_0| \leq |\Delta\nu_{abs}| \\ 0 & \text{everywhere else} \end{cases}, \quad (2)$$

where  $\nu_0$  is the rest frame frequency of the considered transition and

$$\phi_{abs}(\nu - \nu_0, \sigma_{turb}) = \frac{1}{H} \left\{ \frac{1}{\sqrt{\pi}\sigma_{turb}} \exp \left( \frac{-(\nu - \nu_0)^2}{\sigma_{turb}^2} \right) + K \right\}, \quad (3)$$

in which  $K$  ensures a continuous transition between the absorption profile and the zero intensity.  $H$  is a constant allowing for the normalization of the line profile over the interval  $\nu_0 \pm |\Delta\nu_{abs}|/2$ , where  $\Delta\nu_{abs}$  is the full width at zero intensity (FWZI) of the absorption profile. We choose the value of  $\Delta\nu_{abs}$  in order to ensure the continuity of the absorption profile at the border of the interval  $\nu_0 \pm |\Delta\nu_{abs}|/2$ . The parameter  $\sigma_{turb} = \Delta\nu_{turb}/(2\sqrt{2\ln 2})$  is such that  $\Delta\nu_{turb} = 2\nu_0(v_{turb}/c)$  is the FWHM of the absorption profile. The velocity  $v_{turb}$  takes into account the thermal and the macroscopic turbulence components in the wind which broaden the absorption profile (we assume  $v_{turb}$  to be constant throughout the wind).

Due to the velocity field  $\vec{v}(r, \theta, \phi)$  present in the wind, the initial frequency  $\nu_i$  of a photon flying in the direction  $\vec{n}$  is seen Doppler shifted by an atom of the wind in such a way that its “local” frequency  $\nu_l$  in the atom rest-frame is given by:

$$\nu_l = \nu_i \left( 1 - \frac{\vec{v} \cdot \vec{n}}{c} \right). \quad (4)$$

Thus a photon will enter in resonance with the surrounding atoms only if its local frequency fulfills the condition defining the so-called “resonance zone”:

$$\nu_0 - \frac{\Delta\nu_{abs}}{2} < \nu_l < \nu_0 + \frac{\Delta\nu_{abs}}{2}, \quad (5)$$

When the photon enters such a region, the opacity of the medium becomes nonzero and so does the probability of being absorbed. If  $n$  resonance zones are found along the direction of propagation of the photon in the wind, the total optical depth  $\tau_{tot}$  seen by the photon until it escapes the wind is simply computed as:

$$\tau_{tot}(\nu_i) = \sum_{j=1}^n \int_{a_j}^{b_j} \kappa_{\nu_0} \phi_{abs}(\nu_l - \nu_0, \sigma_{turb}) ds, \quad (6)$$

where  $\kappa_{\nu_0}$  is the total absorption coefficient of the considered resonance transition and  $a_j$  and  $b_j$  are respectively the coordinates

of the beginning and of the end of the  $j^{th}$  resonance zone found along the line of flight of the photon.

Given the probabilistic interpretation of the RT, a photon experiencing a total optical depth of  $\tau_{tot}(v_i)$  has a probability  $p = e^{-\tau_{tot}(v_i)}$  of escaping the medium without being absorbed. This interpretation is used in the MC code in order to identify the occurrence and the position of the scattering sites along the path of the photon through the wind. Indeed using the transformation equation (Eq. 1) we can determine the random optical depth  $\tau_{MC}$  at which the photon interacts :

$$\tau_{MC} = -\ln(1 - \xi), \quad (7)$$

As we stored the run of  $\tau_{tot} = \tau_{tot}(s)$  along the photon path, it is easy to invert this relation and find the point  $s$  where  $\tau_{tot} = \tau_{MC}$ . At this location the photon is radiatively absorbed and then instantaneously re-emitted at a frequency and in a direction chosen by assuming a complete redistribution in frequency and direction (CRFD, Lucy 1971, Mihalas et al. 1976). This photon may then either be re-absorbed somewhere else in the wind or leave it and be detected by one of the detector (spectrographs, imagers) located around the wind.

In order to decrease the simulation time in the case of non-spherically symmetric winds we make an intense use of the advanced concepts of “first forced interaction” (e.g. Cashwell & Everett 1959, Witt 1977) and “peeling off” (e.g. Yusef-Zadeh et al. 1984, Wood & Reynolds 1999) where we follow a photon packet rather than a single photon.

We checked the validity of our MCRT code by comparing the line profiles we obtain to line profiles computed with two traditional methods for spherical winds which allow an exact integration of the transfer equation. These benchmarks are the well-known SEI method of Lamers et al. (1987) and the comoving frame method of Hamann et al. (1981). We noted a good agreement between the general shape of the computed profiles whatever the considered turbulence ( $\Delta F/F \leq 5\%$  on the normalized emission peak flux as well as a good match between the absorption profiles). We also tested MCRT in the case of axi-symmetric winds by comparing the profiles obtained with MCRT to those produced by the SEI method adapted by Bjorkman et al. (1994). Once again we observed a good agreement between the line profiles produced by both methods.

### 2.3. Pure emission

While the shape of the C IV line in BAL QSO’s can be mostly governed by resonance scattering (Scargle et al. 1972), the presence of C III] emission constitutes an evidence that part of the emission is due to collisional excitation (Turnshek 1984a, Turnshek 1988, Hamann et al. 1993). In order to account for this second source of photons, we allow the production directly in the wind of a fraction of photons  $f_e = I_{\text{pure emission}}/I_{\text{continuum}}$ . The choice of the location of the emission  $(r_e, \theta_e, \phi_e)$  of these photons is made using a random sampling of the corresponding NPDF:

$$\xi = p(r_e, \theta_e, \phi_e) = \int_0^{\phi_e} \int_0^{\theta_e} \int_{R_{in}}^{r_e} \eta(r, \theta, \phi) r^2 \sin \theta dr d\theta d\phi, \quad (8)$$

where the  $\eta(r, \theta, \phi)$  is a function which describes the emissivity throughout the wind. Once again, our goal here is not to provide a detailed self-consistent model of the wind so we choose as a first guess an emissivity function of the form:

$$\eta(r, \theta, \phi) = n(r, \theta, \phi) \left( \frac{R_{in}}{r} \right)^{\gamma}, \quad (9)$$

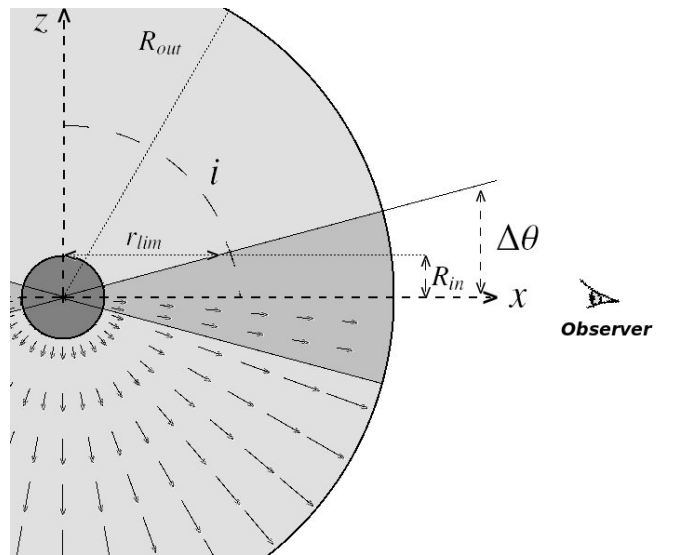


**Fig. 1.** Illustration in the  $x$ - $z$  plane of the two component wind used in our MC simulations, the velocity field is pictured by arrows in the lower part of the picture. The equatorial wind is shown edge-on (in dark grey) so that the wind model is rotationnally symmetric along the  $z$  axis. The viewing angle of the observer is  $i = 90^\circ$ , and the absorption profile is produced by both component, the polar one contributing only at low velocities (i.e. for  $x < r_{lim}$ ) given the disk opening angle and the viewing angle. Inspired from Fig. 8 of Bjorkman et al. (1994).

where  $n(r, \theta, \phi)$  is the density of the ion through the wind and where the second term allows to take the temperature distribution and the ionization fraction into account. In the following we will simply take  $\gamma = 1$  in order to reduce the number of free parameters.

Each photon emitted then follows its way through the wind where it can be scattered and then finally escapes the wind in order to be detected by a distant observer.

### 2.4. The Wind Model

As stated in the introduction, it is difficult to give a simple explanation to the observed BAL profiles when using a spherically symmetric expanding wind. The obvious next type of geometry which can then be considered is the axi-symmetric one. The simplest of such models would still consist in a wind originating from the central core. Such a generic model, with polar and equatorial components, like the one presented in details by Bjorkman et al. (1994), produces line profiles remarkably similar to those observed in some BAL QSOs. Although simple, this model is versatile enough to produce a variety of line profiles, as observed in BAL QSOs. It constitutes a first good approximation to the more complex wind+disk models proposed to explain AGN outflows in which the BALR and the BELR are generally cospatial (Sect. 1). We then decided to implement the model described by Bjorkman et al. (1994) and we remind here its basic characteristics.

The velocity field  $\vec{v}(r, \theta, \phi)$  considered here can be written in spherical coordinates:

$$\vec{v}(r, \theta, \phi) = v_r(r, \theta) \vec{e}_r + v_\phi(r, \theta) \vec{e}_\phi + v_\theta(r, \theta) \vec{e}_\theta, \quad (10)$$

where we assume for simplicity, as in Bjorkman et al. (1994), that the streamlines lie on surfaces of constant polar angle so

that  $v_\theta = 0$ . The radial component of the velocity field has the typical  $\beta$ -law shape:

$$v_r(r, \theta) = v_{\min} + (v_{\max}(\theta) - v_{\min}) \left(1 - \frac{R_{\text{in}}}{r}\right)^\beta, \quad (11)$$

where  $v_{\min}$  is the wind speed at the surface of the source of the continuum and the variable terminal speed  $v_{\max}(\theta)$  allows for the introduction of a slow expanding equatorial wind in a faster polar wind:

$$v_{\max}(\theta) = v_{\max}^{\text{po}} + (v_{\max}^{\text{eq}} - v_{\max}^{\text{po}})f(\theta), \quad (12)$$

where  $v_{\max}^{\text{eq}}$  and  $v_{\max}^{\text{po}}$  are respectively the terminal velocity of the equatorial and the polar components. The function which allows the smooth transition between the two components of the wind is of the form:

$$f(\theta) = 0.5 \left[ 1 + \frac{2}{\pi} \arctan \left( \frac{\sin \Delta\theta - \cos \theta}{\Delta\theta_t} \right) \right], \quad (13)$$

$\Delta\theta$  being the equatorial wind half opening angle and where the parameter  $\Delta\theta_t$  controls the transition between the equatorial and the polar component of the wind. We choose, similarly to Bjorkman et al. (1994), a small value of  $\Delta\theta_t = 0.001$  in order to keep this region much thinner than the equatorial wind opening angle.

The  $v_\phi$  component of the velocity field is simply given by assuming conservation of the angular momentum in the wind:

$$v_\phi = \frac{V_{\text{rot}} R_{\text{in}}}{r} \sin \theta, \quad (14)$$

where  $V_{\text{rot}}$  is the rotational speed at the surface of the source of the continuum.

The law governing the distribution of the ion density is derived from the equation of continuity of matter in a central wind and is parametrized using :

$$n(r, \theta, \phi) = n_0(\theta) \left( \frac{r}{R_{\text{in}}} \right)^{-\alpha} \left( \frac{v_r(r, \theta)}{v_{\min}} \right)^{-1}, \quad (15)$$

the parameter  $\alpha$  implicitly including the radial variation of the ionization (i.e.  $\alpha = 2$  meaning a constant ionization throughout the wind) and  $n_0(\theta)$  allowing the transition between the polar and the equatorial components:

$$n_0(\theta) = n_0^{\text{po}} + (n_0^{\text{eq}} - n_0^{\text{po}})f(\theta), \quad (16)$$

where  $n_0^{\text{eq}}$  and  $n_0^{\text{po}}$  are, respectively, the density of the considered ion at the base of the wind in the equatorial or in the polar component. The value of  $n_0^{\text{po}}$  is computed by specifying the value  $\tau_{\text{tot}_p}$  of the total optical depth of the wind along the polar axis (i.e.  $\theta = 0^\circ$ ) integrated over frequency:

$$\tau_{\text{tot}_p} = \int_{-\Delta\nu_l}^{\Delta\nu_l} \tau_{\text{tot}}(\nu_i) d\nu_i, \quad (17)$$

$2\Delta\nu_l$  being the measured width of the observed line profile. The value of  $n_0^{\text{eq}}$  is fixed by the free parameter  $k_{\text{pm}}$  which defines the ratio of the ionic density between the two components at the base of the wind:

$$n_0^{\text{eq}} = k_{\text{pm}} n_0^{\text{po}}. \quad (18)$$

**Table 1.** Wind parameter for the benchmark model

Parameter	Value	Parameter	Value
$v_{\max}^{\text{po}}$	10000 km s <sup>-1</sup>	$\alpha$	2.00
$v_{\min}$	100 km s <sup>-1</sup>	$\beta$	1.00
$v_{\max}^{\text{eq}}$	2500 km s <sup>-1</sup>	$\Delta\theta$	15°
$V_{\text{rot}}$	0 km s <sup>-1</sup>	$\Delta\theta_t$	0.001
$v_{\text{turb}}$	500 km s <sup>-1</sup>	$i$	90°
$\tau_{\text{tot}_p}$	4.00	$f_e$	0.0
$k_{\text{pm}}$	10.0	$\gamma$	1.0

### 3. Parameter study

Here we concentrate on the main parameters affecting the line profiles in the case of a two component wind where we suppose no pure emission (i.e.  $f_e = 0$ ). We will not discuss the effects of the parameters governing the velocity and density laws or the effects of the turbulent component in the wind since they are similar to those observed in the well-understood spherically expanding wind case (Castor & Lamers 1979, Beckwith & Natta 1987, Hamman 1981, Lamers et al. 1987).

The most important parameters we have to specify in order to compute a line profile are: the frequency integrated polar optical depth  $\tau_{\text{tot}_p}$ , the ratio between the equatorial and the polar ionic density  $k_{\text{pm}}$ , the velocity ratio between the polar and the equatorial terminal speed  $v_{\max}^{\text{eq}}/v_{\max}^{\text{po}}$ , the disk half-opening angle  $\Delta\theta$ , the viewing angle  $i$  and the ratio  $V_{\text{rot}}/v_{\max}^{\text{po}}$  between the rotational speed of the source of continuum and the polar terminal velocity. The parameters used for the reference line profile are summarized in Table 1. Such a parameter study was previously carried out by Bjorkman et al. (1994) using a SEI-type method. As their calculations agree with those we obtained using an exact method, we will only remind here the general effects produced by each parameter and refer the reader to Bjorkman et al.'s paper for further details. We will however emphasize the effect of the wind rotation given the important changes in the line profile produced by the variation of this parameter, more particularly when the equatorial disk is viewed near edge-on (Mazzali 1990, Petrenz & Puls 1996, Busche & Hillier 2005).

The profiles illustrated in the panel A of Fig.2 are representative of the profiles that can be produced in a two-component wind when the equatorial wind is seen near edge-on. The shape of these profiles are constituted of a typical P Cygni-like profile extending to the higher velocities coming from the polar component, but where a sharp absorption trough is produced at smaller velocities by the slow expanding equatorial wind. In this panel we illustrate the evolution of the line profiles as a function of the total polar optical depth integrated over frequencies  $\tau_{\text{tot}_p}$ . Similarly to the spherically symmetric expanding wind case (e.g. the atlas constructed by Castor & Lamers 1979), when  $\tau_{\text{tot}_p}$  is increased, we observe an increase of the emission peak and of the equivalent width of both the emission and absorption parts of the line profile. No variations are observed in the equatorial absorption since that part of the profile is already saturated for the smaller value of  $\tau_{\text{tot}_p}$ .

The effect of the  $k_{\text{pm}}$  ratio is illustrated in the panel B of Fig. 2. When  $k_{\text{pm}}$  is decreased, the depth of the absorption profile of the equatorial component evolves in the same way. As Bjorkman et al. (1994) we observe that the equatorial component is still optically thicker to the radiation than the polar component even for  $k_{\text{pm}} = 0.1$  and this because of the smaller velocity range of the equatorial component.

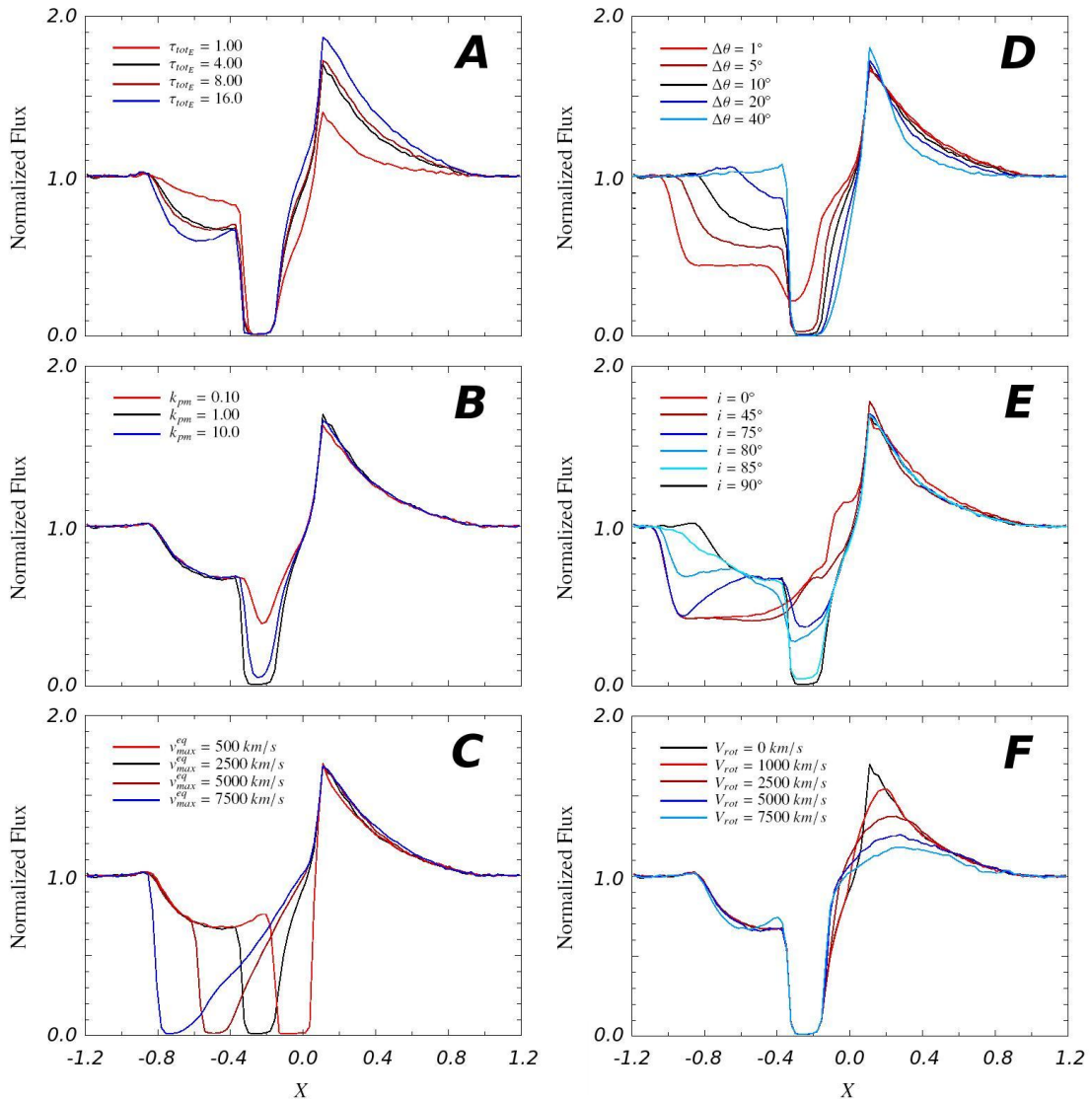


**Fig. 2.** Illustration of the effects of the wind's main parameter on the line profile (see text for details). Each spectrum is represented as a function of the normalized wavelength  $X = (\lambda - \lambda_0)/(\lambda_{max} - \lambda_0)$  and is the result of the simulation of  $2 \cdot 10^6$  photon paths through the wind ( $S/N > 100$  on the continuum level).

The change of the ratio between the terminal speed  $v_{max}^{eq}$  and  $v_{max}^{po}$  of the two components essentially modifies the position of the edge of the low velocity absorption component (see panel C of Fig. 2). We also observe that when  $v_{max}^{eq}$  is increased, the absorption due to the presence of the disk remains no longer black near the line center. Indeed in order to produce a black absorption, the disk has to cover the whole source of continuum. But for an equatorial wind with a half-opening angle  $\Delta\theta$ , this only happens beyond the radial coordinate  $r > r_{lim} = R_{in} \cotan\Delta\theta$  (see Fig. 1) which corresponds to the velocity  $v_{lim}^{eq} \sim v_r(r_{lim}, 90^\circ)$  the value of which is sensitive to  $v_{max}(\theta)$  (cf. Eq. 11).

In the panel D of Fig. 2 we illustrate the evolution of the line shape as a function of the half opening angle of the equatorial wind  $\Delta\theta$ . We observe the apparition of a broad high velocity absorption when  $\Delta\theta$  is decreased. This observation is once more explained by considering the radial coordinate  $r_{lim}$  at which the disk completely covers the source of the continuum. As the high velocity absorption (due to the polar component) occurs before the equatorial wind, the high absorption velocity range is limited

within the interval  $[0, v_{lim}^{po}]$ , where  $v_{lim}^{po} \sim v_r(r_{lim}, 0^\circ)$ . In contrast, when  $\Delta\theta$  is increased, we observe the apparition of a secondary blueshifted emission peak beyond  $v_{max}^{eq}$  given the fact that for a sufficiently wide disk there is no remaining polar absorption of the continuum.

The viewing angle  $i$  to the wind plays a critical role in the line profile (see panel E of Fig. 2). Indeed the equatorial absorption component is only seen when the disk is viewed near edge-on (i.e.  $i = 90^\circ$ ). As  $i$  is decreased from an edge-on to a pole-on ( $i = 0^\circ$ ) view of the disk, the low velocity absorption produced by the disk decreases since only the high velocity end of this component covers the continuum.

Finally panel F of Fig. 2 illustrates the modifications of the line profile when varying the rotational speed of the wind. The major effect of the rotation is observed on the emission peak which decreases and is significantly redshifted when the  $V_{rot}/v_{max}^{po}$  ratio is increased. Indeed, when there is no rotation, the emission peak is relatively sharp because that part of the profile is produced in the inner, optically thicker, regions of the wind,

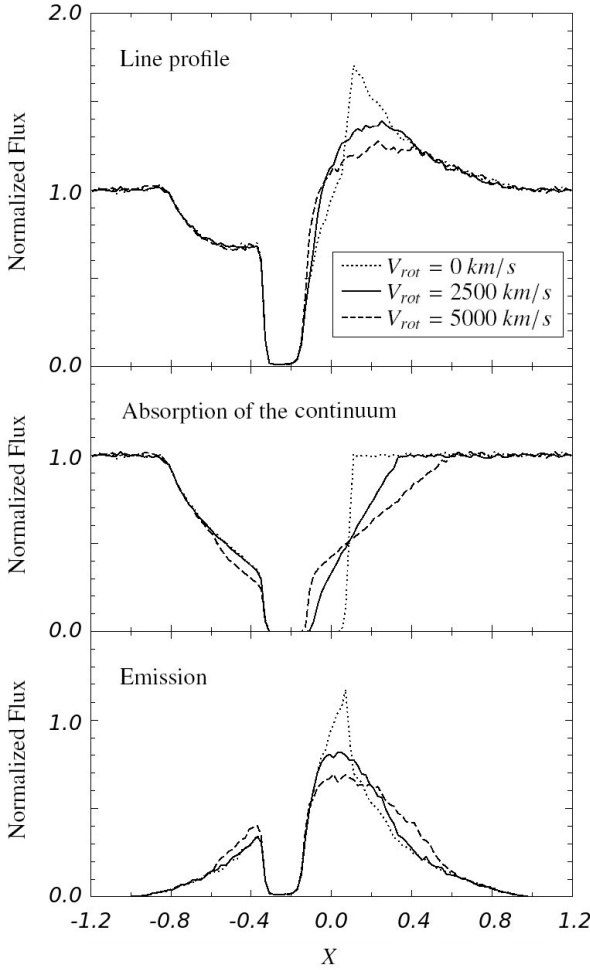


**Fig. 3.** Closer illustration of the effect of the rotation of the wind over the line profile, its part in emission and its part in absorption. The dotted line represents the profiles for which the rotational velocity is null while the straight line represents the profiles with  $V_{\text{rot}} = 0.25 v_{\text{max}}^{\text{eq}}$ , and the dashed line a wind where  $V_{\text{rot}} = 0.50 v_{\text{max}}^{\text{eq}}$ . The parameter used are those gathered in Table 1. When the rotation is increased, we observe the apparition of an absorption component in the red side of the line profile simultaneously with a decrease of the absorption in the blue part since the continuum emitting region is no longer completely covered with optically thick material (see text).

whose velocity range is small. When rotation is considered the resonance zones become twisted in such a way that the inner regions are distributed over a wider range of projected velocity. This induces the smoothening of the emission peak since the rotation allows the absorption to occur in the redder part of the continuum at frequencies centered on the rest-frame frequency of the line transition  $v_0$  (e.g.  $X = 0.0$ ) (see Fig. 3 and also Hall et al. 2002 for a detailed explanation). The bluer part of the absorption profile is not significantly affected by the rotation because this part of the profile is produced in front of the continuum source, i.e. where the projected rotational velocity is nearly null. While the rotation of the wind produces important modifications of the line profile, Mazzali et al. (1990) showed that the introduction of such a component does not significantly affect the dynamical (mass loss rate,  $v_r(r, \theta)$ ) nor the ionization properties of the wind.

#### 4. Fitting BAL profiles with the wind+disk model

In this section we try to reproduce a selection of representative C IV line profiles observed in BAL QSOs and extracted from the paper of Korista et al. (1993) which provides homogeneous and high-quality spectroscopic data for a large sample of BAL QSOs. Our goal is to check if such profiles can be modelled using a simple two component wind geometry for the BALR. Ten spectra were carefully selected out of the 72 BAL QSOs presented in Korista et al.'s paper on the basis of two criteria :

- we retained as far as possible objects free of doublet effects (i.e.  $v_{\text{max}}^{\text{po}} \gg \text{C IV doublet separation}$ ), non-blended and with smooth emission/absorption C IV line profile (i.e those less affected by multiple absorption troughs).
- we selected objects for which the continuum can be securely defined on both side of the C IV line profile, allowing for a correct normalization of the spectra.

The observed and the fitted spectra of each selected object are illustrated, normalized to the continuum level, in Figs. 4 and 5. The parameters used in the fit of each C IV line profile are gathered in Table 2. While some parameters ( $v_{\text{max}}^{\text{eq}}, v_{\text{max}}^{\text{po}}, i, \tau_{\text{tot}, p}, \alpha, f_e, \dots$ ) were allowed to vary, we tried to keep fixed the radial velocity gradient in the wind (the  $\beta$  parameter), the emission parameter  $\gamma$  and the disk opening angle  $\Delta\theta$ . The latter was chosen equal to the value generally adopted for the opening angles of disk winds in AGN models (Murray et al. 1995, Proga & Kallman 2004). However, even those parameters were varied in a few cases in order to slightly modify the part of the profile in emission. In particular, we found that the opening angle  $\Delta\theta$  of the disk has to be decreased for fitting the high velocity absorption component (see Sect. 3) observed in the P Cygni-type line profiles (Q1333+2840 and Q1413+1143).

The sample contains various types of BAL spectra, from the P Cygni-type to the more complex profiles discussed in the paper of Korista et al. (1993). This subdivision of BAL QSO spectra was introduced by Turnshek (1984b) and based on the visual properties of the BAL profiles, where the P Cygni-like profiles with a smooth absorption and a high emission peak relative to the continuum level are distinguished from the complex/detached absorption ones with a lower emission peak. However we tried to model all these line profiles using the same wind geometry since, as suggested by Turnshek (1984b), it is likely that distinct types of BAL profiles are the consequence of a unique mass-loss phenomenon.

The empirical fitting procedure we adopted here makes the distinction between three types of line profiles, each possessing its own set of spectral signatures. The first kind of line profiles are the P Cygni-like ones (Q1333+2840 and Q1413+117 see top panels of Fig. 4). In this subsample, the absorption trough seems to be constituted of two subtroughs covering two overlapping velocity ranges, i.e. an optically thick “narrow” ( $\sim 4000 \text{ km s}^{-1}$  wide) absorption component superimposed on an optically thin absorption trough extending up to velocities of  $10000 \text{ km s}^{-1}$ . This signature suggests the presence of an equatorial denser disk seen nearly edge-on producing the narrow absorption observed. The necessity of considering such a slower expanding disk in a polar wind is particularly well illustrated when observing the C IV line profile of Q1413+117. In this object, the absorption profile extends to velocities up to  $-10000 \text{ km s}^{-1}$  which implies, through resonance scattering, the presence of an underlying emission component extending from  $-10000 \text{ km s}^{-1}$  to  $10000 \text{ km s}^{-1}$ . Since the flux is almost zero at smaller velocities ( $v \leq 4000 \text{ km s}^{-1}$ ), a part of these photons have to be re-absorbed some-

**Table 2.** Parameter of the two-component wind model for the best fit of the C IV BALs in the selected quasar sample.

BAL QSO Name	$z$	$\tau_{tot_p}$	$k_{pm}$	$v_{max}^{po}$ (km s $^{-1}$ )	$v_{max}^{eq}$ (km s $^{-1}$ )	$V_{rot}$ (km s $^{-1}$ )	$\alpha$	$\beta$	$\Delta\theta$ ( $^{\circ}$ )	$i$ ( $^{\circ}$ )	$f_e$	$\gamma$
Q1333+2840	1.897	3.00	10.0	13000	4000	1000	3.0	0.8	10	80	0.21	1.0
Q1413+1143	2.522	10.0	15.0	11000	3500	2000	3.0	0.8	10	88	0.16	1.0
Q0145+0416	1.990	1.00	12.0	18000	9600	6400	2.5	1.2	15	80	0.18	1.0
Q0226-1024	2.164	1.00	10.0	25000	12500	12500	2.0	1.5	15	87	0.10	1.0
Q0321-3344	1.955	10.0	10.0	10000	7500	5200	2.5	1.5	15	75	0.16	1.0
Q0842+3431	2.100	14.0	5.00	16000	10000	8000	3.0	1.5	15	78	0.04	1.0
Q1235+1453	2.835	5.00	10.0	13000	8000	7000	2.5	1.5	15	76	0.12	1.0
Q1239+0995	1.970	3.00	5.00	16000	8000	8000	3.0	1.0	15	82	0.10	1.0
Q0019+0107 M1	2.075	1.00	15.0	16000	9000	8000	2.5	1.5	15	90	0.11	1.0
Q0019+0107 M2	2.075	0.00	15.0 <sup>a</sup>	-	9000	8000	2.5	1.5	15	90	0.11	1.0
Q0041-4023 M1	2.450	5.00	10.0	10000	5000	3000	2.0	1.5	15	90	0.18	1.0
Q0041-4023 M2	2.450	15.0	5.0	6000	3000	3000	2.0	0.5	15	0	0.07	1.0

<sup>a</sup> In this case  $k_{pm}$  represents the total equatorial ( $i = 90^{\circ}$ ) optical depth integrated over frequencies since  $\tau_{tot_p} = 0$ .

where else, suggesting the presence of an optically thicker region on the line of sight to the observer in agreement. This observation fits the framework in which a part of the emission from the BELR is absorbed in the BALR (e.g. Turnshek et al. 1988, Hamann et al. 1993).

The second type of line profiles we considered are those presented in the lower panels of Fig. 4. They are characterised by an asymmetric emission peak whose intensity relative to the continuum level is significantly lower than in the P Cygni-type ones. Some individuals of this subsample also show, similarly to the P Cygni-like ones, the presence of a higher velocity absorption trough component superimposed to a narrower component (best seen in e.g. Q0842+3431, Q1235+1453). For these objects the introduction of a significant rotation of the wind around the polar axis is required in order to produce the broad asymmetric emission peaks observed in the C IV line profile of seven out of the ten objects of our sample (Q0019+0107, Q0145+416, Q0226-1024, Q032-3344, Q0842+3431, Q1235+1453 and Q1239+0995). The rotational speed generally needs to be quite high relative to the polar terminal velocity (reaching up to 50 % of  $v_{max}^{po}$ ) and is approximately equal to the equatorial wind terminal velocity. Note that for the P Cygni-like profiles (Q1333+2840, Q1413+1143 or even Q0041-4023) it is also necessary to consider the rotation of the wind around the polar axis, but it must be smaller to account for the higher emission peak and the sharp transition between the emission and the absorption parts of the profiles.

In each case, the best fit was chosen by eye, once the model was qualitatively similar to the profile of the observed line. The simulation time needed to produce a single line profile in these optically thick winds prevents us from using a  $\chi^2$  type technique while searching for the best model. However this is not a main drawback since our main goal is to show that a simple wind model is able to approximately reproduce a variety of resonance line profiles observed in BAL QSOs. Moreover, given the degeneracy between some of the model parameters ( $k_{pm} - i$ ,  $v_{max}^{eq} - i$ ,  $\beta - \alpha$ , etc), as well as the difficulty in some cases to evaluate correctly  $v_{max}^{po}$  or other model parameters, more than one best fit is generally possible.

The absence of the two-component wind signatures defined above in the C IV line profile of some objects led us to define a third subsample of line profiles. These line profiles can still be fitted by using a two-component wind (see upper panel of Fig. 5). However, some profiles (the prototype being Q0019+0107) do not show evidence for a polar absorption component at high velocities, suggesting that the polar outflow may not be present

in some objects. Several tests performed on such line profiles with MCRT showed that Q0019+0107-type line profiles can also be produced in a single rapidly rotating equatorial wind seen nearly edge-on (see lower left panel of Fig. 5). In the same way, in the bottom right panel of Fig. 5, we illustrate how the C IV line profile of Q0041-4023 can be reproduced by a 2-component wind seen nearly pole-on. This arises when a single deep absorption trough is observed associated with a quasi-symmetric emission profile. Once again given the uncertainties on several wind parameters due to the lack of clear signatures in the line shape, several wind model can be fitted to the observed line profiles (here we choose for M2  $v_{max}^{eq} = V_{rot} = 0.5 v_{max}^{po}$  as typical values).

From Figs. 4 and 5 we note that our simple model is able to reproduce quite well the diversity of the BAL profiles observed in a real sample of objects. Interestingly enough in order to be able to fit the C IV profiles with MCRT, we must shift the whole simulated line profile with respect to the emission peak, usually used for redshift determination. This shift is needed to center on the zero velocity the underlying emission component of the profile. Indeed when dealing with resonant scattering, an absorption trough extending on the velocity range  $[0, -v_{max}]$  produces an emission feature extending from  $-v_{max}$  to  $+v_{max}$ . The redshifts of the quasar C IV determined from the center of the underlying emission line are given in the second column of Table 2.

From the fitting procedure, we note that one of the major parameters which control the line profile in this type of wind remains the viewing angle  $i$ , which plays a crucial role on the shape of the absorption part of the line by controlling the relative contribution of the equatorial wind and polar components (when both are required). Thus when a line profile exhibits a sharp, deep absorption trough superimposed on a shallower high velocity absorption component, the quasar is probably viewed along a line of sight such as the dense equatorial wind is seen nearly edge-on (e.g. Q1413+117). However it should be kept in mind that an edge-on disk does not necessarily produce a completely black absorption trough even for the highest optical depths (cf. Table 2) since photons are scattered in the line of sight to the observer and may not be completely reabsorbed by the disk filling in the absorption trough. This is in agreement with what is usually observed among the Korista et al. (1993) spectra and was already pointed out in Lee & Blandford (1997) or Arav et al. (2007, and references therein)

Finally we note that in all modeled profiles, we need to allow the creation of photons inside the wind (a fraction  $f_e > 0$  relative to the continuum intensity). This intrinsic emission pro-

duces stronger emission peaks than in the case of a purely resonant scattering atmosphere.

## 5. Discussion

We showed that a simple two-component equatorial+polar wind model is able to reproduce a variety of BAL profiles, ranging from detached absorption troughs to P Cygni-like profiles. The solutions of the fits are not unique and several models with different geometries and/or physical properties can equally reproduce the observed spectra. In accordance with previous studies (e.g. Hamann et al. 1993), this demonstrates that a unique physical characterization of the outflow cannot be derived from line profile fitting.

While detailed information on the geometry of the outflows cannot be derived, we nevertheless reached some interesting conclusions. First, in some objects, it is necessary to include both the disk and the polar absorption region. This is indeed the case for objects like Q1413+117, Q1333+2840 but also Q1235+1453 or Q0842+3431 where the polar component allows to reproduce the shallow absorption trough observed at higher velocities. In other objects (the prototype in our sample being Q0019+0107), the lack of that high velocity signature suggests that the presence of the polar component is not necessary at all so that the profile can then be fitted with a single rapidly rotating equatorial wind seen nearly edge-on.

Interestingly, the viewing angle to the wind in each of the fitted spectra is generally found to be high suggesting at first sight that BAL quasars are essentially observed when the optically thick equatorial wind blocks the direct view to the continuum source. This is in agreement with the high viewing angle generally inferred in order to account for the spectropolarimetric properties of BAL QSOs (Schmidt & Hines 1999, Ogle et al. 1999). The fact that the polar component can be omitted in some cases favors such a scheme in which only a fraction of the continuum source is covered by the BAL material, in agreement with the unification by orientation model of BAL QSOs and non-BAL QSOs (e.g. Turnshek 1984a, Hamann et al. 1993). However, we showed for Q0041-4023 that when the line profile is constituted of a single deep absorption trough and a quasi-symmetric emission peak, the line profile can also be produced in a two-component wind seen pole-on (see the bottom right panel of Fig. 5). This result underlines the fact that some BAL troughs can also be observed as the result of a polar outflow in a two-component wind, with a large covering factor. As mentioned in Sect. 1 a growing number of radio data observations of BAL QSOs provides evidence for such two-component wind models while recent hydrodynamical simulations showed that a stable two-component wind can result from the flow around a black hole and its accretion disk (e.g. Proga 2007).

In our study we decided to use a simple central wind model including an equatorial and a polar component. Such a simple model proved that this type of wind can account for most characteristics of the resonance line profiles observed in the spectra of BAL QSOs. However we were not able to reproduce the C<sub>IV</sub> line shape of the P Cygni class prototype PHL5200. This indicates that the model used does not include all the ingredients needed. Indeed this model can not reproduce the very sharp transition observed between the absorption and the emission component in the C<sub>IV</sub> line profile of PHL5200 (Turnshek et al. 1988). Such a sharp transition at zero velocity could in turn be produced in a wind launched from the disk itself. In that type of model, which exhibits large scale properties similar to those of the wind model considered in the present study, the wind is launched from the

**Table 3.** Blueshift of the C<sub>IV</sub> line relative to the systemic redshift  $z_{\text{sys}}$  for the three quasars from our sample with secured [O III] line measurement.

BAL QSO Name	$z_{\text{sys}}$	Ref. $z_{\text{sys}}$	$\Delta v_{\text{blueshift}}$
Q0019+0107	2.131	Dietrich et al. 2009	5500 km s <sup>-1</sup>
Q0226-1024	2.268	McIntosh et al. 1999	9200 km s <sup>-1</sup>
Q1413+1143	2.553	Hutsemékers et al. 2009	2500 km s <sup>-1</sup>

disk and then accelerated away by the radiation pressure (Murray et al. 1995, Proga & Kallman 2004). When observed near edge-on, it can produce a strong absorption at the center of the line such as that observed in PHL5200. The implementation of that type of wind is beyond the scope of this paper and will be discussed in a future paper.

Furthermore, in a majority of objects we found necessary to use large values of the ratio  $V_{\text{rot}}/v_{\text{max}}^{\text{po}}$  of the rotational speed to the polar terminal speed of the wind to adequately reproduce the asymmetry of the emission line profiles. Such a large value of the rotation accounts for the redshift and the faintness of the emission peak. These characteristics results from the fact that when rotation is present, the continuum light emitted on the red side of the line profile can be absorbed by the optically thick material located between the source of continuum and the distant observer (see Fig. 3). The rotational velocity at the base of the wind can reach several thousand km s<sup>-1</sup>, which is consistent with the rotational velocities inferred for gas orbiting in the vicinity of a supermassive black hole (e.g. Murray et al. 1995, Young et al. 2007). Interestingly, we found that the rotational velocity must remain small in quasars with P Cygni-like line profiles, suggesting a possible dynamical difference between the BAL QSOs with detached profiles and those ones with P Cygni-type profiles. The rotation of the wind naturally provides a simple and straightforward interpretation of the correlation between the properties of the Broad Emission Lines (BELs) and those of the Broad Absorption Lines as reported by Turnshek (1984a). Indeed, as shown in that paper, BAL QSOs having complex absorption generally have a smaller C<sub>IV</sub> emission peak relative to the continuum than does BAL QSOs with smooth P Cygni absorption. This can be explained by the stronger/wider absorption on the red side of the line profile resulting from the rotation of optically thick material in front of the continuum source. Combining the emission profile and the redshifted absorption of the continuum results in profiles resembling to the so-called detached troughs observed in a number of BAL QSO spectra (Korista et al. 1993, Arav & Begelman 1994, Hall et al. 2002, Proga & Kallman 2004). Recently, spectropolarimetry of the BAL QSO PG1700+518 revealed significant variations of the polarization position angle over the H $\alpha$  and H $\beta$  BAL troughs which is interpreted as a typical signature of a rotating wind (Young et al. 2007, Wang et al. 2007).

When fitting the C<sub>IV</sub> line profiles, we found necessary to adopt a systemic redshift for the wind smaller than the redshift given by the peak of the C<sub>IV</sub> emission line. This “wind redshift” corresponds to the centroïd of the full emission component which underlies the observed absorption+emission profile and defines the rest-frame of the outflow model. It is interesting to compare this redshift to the redshift determined from the narrow forbidden lines usually thought to provide the true systemic redshift of the quasar and its host galaxy (e.g. McIntosh et al. 1999, Vanden Berk et al. 2001). Unfortunately only few measurements are available due to the fact that the [O III] lines are shifted in the near-infrared and are fainter in BAL QSOs

than in non-BAL QSOs (Yuan et Wills 2003). For the BAL QSO of our sample, only three accurate determinations are available and are given in Table 3. For these quasars, we find a net blueshift of the simulated C IV line profiles by several thousands of  $\text{km s}^{-1}$  with respect to the systemic redshift measured from [O III]. Such a blueshift of the highly ionized species relative to the narrow [O III] lines –or to the low ionization Mg II line– is rather common and well known in the case of both the BAL and non-BAL QSOs (e.g. Gaskell 1982, Corbin 1990, McIntosh et al. 1999), reaching up to  $4000 \text{ km s}^{-1}$  (Corbin 1990). BAL QSOs are among the QSOs with the largest blueshifts (Richards et al. 2002, 2008), in agreement with our measurements. While the existence of a blueshift of the C IV emission with respect to [O III] emission is well documented, its origin is still unclear. Several mechanisms have been proposed to interpret it, including dust attenuation of the red emission component, scattering of the line profile, relativistic effects, etc. (cf. Corbin 1990, McIntosh et al. 1999, Vanden Berk et al. 2001). Ultimately, it might be necessary to take into account such effects for a full self-consistent modelling of quasar outflows. In the particular case of Q0019+0107, two narrow C IV absorption lines are observed at  $-3000$  and  $+3000 \text{ km s}^{-1}$  in the wind rest frame (Fig. 4), i.e. at  $-8000$  and  $-2000 \text{ km s}^{-1}$  in the systemic quasar+host rest-frame. These velocities suggest that they originate in a large scale outflow in the host galaxy rather than in the BAL wind. Interestingly enough, the velocity difference between these narrow absorption lines is close to the velocity separation between the Ly $\alpha$  and NV resonance doublets ( $\sim 5900 \text{ km s}^{-1}$ ), possibly suggesting a line locking effect (Korista et al. 1993, Arav & Begelman 1994).

## 6. Conclusions

In this study, we used a combination of a Monte Carlo Radiative Transfer code and a simple two-component polar+equatorial wind model to reproduce typical C IV resonance line profiles selected from a homogeneous sample of BAL QSOs spectra.

Although the non-uniqueness of the fits over single line profiles does not allow us to strongly constrain the geometry of the wind, we can summarize our main findings as follows:

1. The diversity of BAL profiles produced by the adopted polar+equatorial model ranges from the typical P Cygni ones to the detached absorption ones similarly to those observed in a homogeneous sample of BAL QSOs.
2. While in some cases the line profiles can be reproduced by a single equatorial wind, we find necessary to use a two-component polar+equatorial wind in a majority of objects.
3. The viewing angle to the wind is generally large (disk seen near edge-on). However in some cases, the line profiles can also be reproduced when assuming a pole-on view, in accordance with the results of recent radio surveys of BAL QSOs.
4. The equatorial wind is rotating and the rotational velocity at the base of the wind can reach a significant fraction of the polar terminal speed.
5. We confirm the findings of Arav (1997) that high optical depth does not imply a black absorption profile since a significant part of the photons can be scattered along different paths in the direction of the distant observer. The depth of the BAL can then not be used securely to derive column densities along the line of sight.

A possible way to break the degeneracy between the various parameter combinations of the two-component model which can reproduce the observed BAL profiles is the use of gravitational

microlensing reported in some lensed systems. Indeed, a microlens moving across the quasar inner regions can differentially magnify the different line forming regions, inducing line profile variations from which the geometry of the outflow can in principle be retrieved. Our code MCRT has been explicitly build up to integrate such microlensing effects. The effect of microlensing on BAL profiles, their use for deriving the physical properties of the outflow, as well as application to a known lensed system will be presented in a second paper.

## References

- Arav, N. & Begelman, M. C. 1994, ApJ, 434, 479  
 Arav, N. 1997, ASP Conf. Ser., 128, 208  
 Arav, N., Becker, R. H., Laurent-Muehleisen, S. A., Gregg, M. D., White, R. L., Brotherton, M. S. & de Kool, M. 1999, ApJ, 524, 566  
 Arav, N., Gabel, J. R., Korista, K. T., Kaastra, J. S., Kriss, G. A., Behar, E., Costantini, E., Gaskell, C. M., Laor, A., Kodituwakku, C. N., Proga, D., Sako, M., Scott, J. E. & Steenbrugge, K. C. 2007, ApJ, 658, 829  
 Avery, L. W. & House, L. L. 1968, ApJ, 152, 493  
 Barlow, T. A., Hamann, F. & Sargent, W. L. W. 1997, ASPC, 128, 13  
 Becker, R. H., White, R. L., Gregg, M. D., Brotherton, M. S., Laurent-Muehleisen, S. A. & Arav, N. 2000, ApJ, 538, 72  
 Beckwith, S. & Natta, A. 1987, A&A, 181, 57  
 Bjorkman, J. E. & Cassinelli, J. P. 1993, ApJ, 409, 429  
 Bjorkman, J. E., Ignace, R., Tripp, T. M. & Cassinelli, J. P. 1994, ApJ, 435, 416  
 Brotherton, M. S., De Breuck, C. & Schaefer, J. J. 2006, MNRAS, 372, 58  
 Brotherton, M. S. 2007, PASP, 373, 315  
 Busche, J. R. & Hillier, D. J. 2005, AJ, 129, 454  
 Cashwell, E. D. & Everett, C. J. 1959, A Practical Manual on the Monte Carlo Method for Random Walk Problems, (New York: Pergamon Press)  
 Castor, J. I. & Lamers, H. G. J. L. M. 1979, ApJS, 39, 481  
 Corbin, M. R., 1990, ApJ, 357, 346  
 Dijkstra, M., Haiman, Z. & Spaans, M. 2006, AJ, 649, 14  
 Dietrich, M., Smita, M., Grupe, D. & Komossa, S. 2009, astro-ph/0901.3378.v2  
 Elvis, M. 2000, ApJ, 545, 63  
 Eracleous, M. & Halpern, J. P. 2003, ApJ, 599, 886  
 Foltz, C., Wilkes, B., Weymann, R. & Turnshek, D. A. 1983, PASP, 95, 341  
 Gallagher, S. C., Brandt, W. N., Sambruna, R. M., Mathur, S. & Yamasaki, N. 1999, ApJ, 519, 549  
 Gallagher, S. C., Hines, D. C., Blaylock, M., Priddey, R. S., Brandt, W. N. & Egami, E. E. 2007, ApJ, 665, 157  
 Ganguly, R., Brotherton, M. S. 2008, ApJ, 672, 102  
 Gaskell, C. M. 1982, ApJ, 263, 79  
 Ghosh, K. K. & Punsly, B. 2007 ApJ, 661, 139  
 Grinin, V. P. 1984, Afz, 20, 190  
 Hall, P. B., Anderson, S. F., Strauss, M. A., York, D. G., Richards, G. T. et al. 2002, ApJS, 141, 267  
 Hamann, W. R. 1981, A&A, 93, 353  
 Hamann, F., Korista, K. T. & Morris, S. L. 1993, ApJ, 415, 541  
 Hazard, C., Morton, D. C., Terlevich, R. & McMahon, R. 1984, ApJ, 282, 23  
 Hewitt, T. G. & Noerdlinger, P. D. 1974, AJ, 188, 315  
 Hutsemékers, D. & Surdej, J. 1990, ApJ, 361, 367  
 Hutsemékers, D., Lamy, H., Remy, M. 1998, A&A, 340, 371  
 Hutsemékers, D., Borguet, B., Sluse, D., Riaud, P. & Anguita, T. 2009, submitted  
 Knigge, C., Woods, J. A. & Drew, J. E. 1995, MNRAS, 273, 225  
 Korista, K. T., Voit, M. G., Morris, S. L. & Weymann, R. J. 1993, ApJS, 88, 357  
 Lamers, H. J. G. L. M., Cerruti-Sola, M. & Perinotto, M. 1987, ApJ, 314, 726  
 Lamy, H. & Hutsemékers, D. 2004, A&A, 427, 107  
 Lee, H.-W. & Blandford, R. D. 1997, MNRAS, 288, 19  
 Knigge, C., Scaringi, S., Goad, M. R. & Cottis, C. E. 2008, MNRAS, 368, 1426  
 Lucy, L. B. 1971, AJ, 163, 95  
 Mazzali, P. A. 1990, A&A, 238, 191  
 McIntosh, D. H., Rix, H.-W., Rieke, M. J. & Foltz, C. B. 1999, ApJ, 517, L73  
 Moore, R. L. & Stockman, H. S., 1984, ApJ, 279, 465  
 Mihalas, D., Kunasz, P. B. & Hummer, D. G. 1976, AJ, 210, 419  
 Murray, N., Chiang, J., Grossman, S. A. & Voit, G. M. 1995, ApJ, 451, 498  
 Murray, N., & Chiang, J. 1997, ApJ, 474, 91  
 Natta, A. & Beckwith, S. 1986, A&A, 158, 310  
 Ogle, P. M., Cohen, M. H., Miller, J. S., Tran, H. D., Goodrich, R. W. & Martel, A. R. 1999, ApJS, 125, 1  
 Pereyra, N. A., Owocski, S. P., Hillier, D. J., Turnshek, D. A. 2004, ApJ, 608, 454  
 Petrenz, P. & Puls, J. 1996, A&A, 312, 195  
 Popovic, L. C., Mediavilla, E., Bon, E. & Ilic, D. 2004, A&A, 423, 909  
 Bon, E., Popovic, L. C., Ilic, D. & Mediavilla, E. 2006, New A Rev., 50, 716

- Press, W. H., Teukolsky, S. A., Vetterling, W. T. & Flannery, B. P. 1992,  
Numerical  
Proga, D. 2003, ApJ, 585, 406  
Proga, D. & Kallman, T. R. 2004, ApJ, 616, 688  
Proga, D. 2007, ApJ, 661, 693 Recipes in FORTRAN - The Art of Scientific  
Computing, 2nd. ed. (New York: Cambridge Univ. Press)  
Reichard, T. A., Richards, G. T., Hall, P. B., Schneider, D. P., Vanden Berk, D.  
E., Fan, X., York, D. G., Knapp, G. R. & Brinkmann, J. 2003, AJ, 126, 2594  
Richards, G. T., Vanden Berk, D. E., Reichard, T. A., Hall, P. B., Schneider, D.  
P., SubbaRao, M., Thakar, A. R. & York, D. G. 2002, AJ, 124, 1  
Richards, G. T. 2008, astro-ph/0603827v1  
Scargle, J. D., Caroff, L. J. & Noerdlinger, P. D. 1972, IAU Symp, 44, 151  
Schmidt, G. D. & Hines, D. C. 1999, ApJ, 512, 125  
Tefler, R. C., Kriss, G. A., Zheng, W., Davidsen, A. F. & Green, R. F. 1998, ApJ,  
509, 132  
Turnshek, D. A. 1984, ApJ, 278, L87  
Turnshek, D. A. 1984, ApJ, 280, 51  
Turnshek, D. A. 1988, "QSO Absorption Lines: Probing the Universe",  
Cambridge University Press  
Turnshek, D. A., Grillmair, C. J., Foltz, C. B., Weymann, R. J. 1988, ApJ, 325,  
651  
Vanden Berk, D. E., Richards, . T., Bauer, A., Strauss, M. A., Schneider, D. P.,  
Heckman, T. M., York, D. G., Hall, P. B., Fan, X., Knapp, G. R. and 52  
coauthors 2001, AJ, 122, 549  
Wang, H.-Y., Wang, T.-G. & Wang, J.-W. 2007, ApJ, 168, 195  
Weymann, R. J., Morris, S. L., Foltz, C. B. & Hewett, P. C. 1991, ApJ, 373, 23  
Witt, A.N. 1977, ApJS, 35, 1  
Wood, K. & Reynolds, R.J. 1999, ApJ, 525, 799  
Wood, K., Whitney, B., Bjorkman, J. E. & Wolff, M. 2001, "Introduction to  
Monte Carlo Radiation Transfer"  
Yamamoto, T. M. 2002, IAUS, 187, 240  
Young, S., Axon, D. J., Robinson, A., Hough, J. H. & Smith, J. E. 2007, Nature,  
450, 74  
Yuan, M. J. & Wills, B. J. 2003, ApJ, 593, L11  
Yusef-Zadeh, C. N. & Burns, P. J. 1999, Random Number Generator  
Recommendation, Colorado State Univ.  
Zhou, H., Wang, T., Wang, H., Wang, J., Yuan, W., & Lu, Y. 2006, ApJ, 639, 716

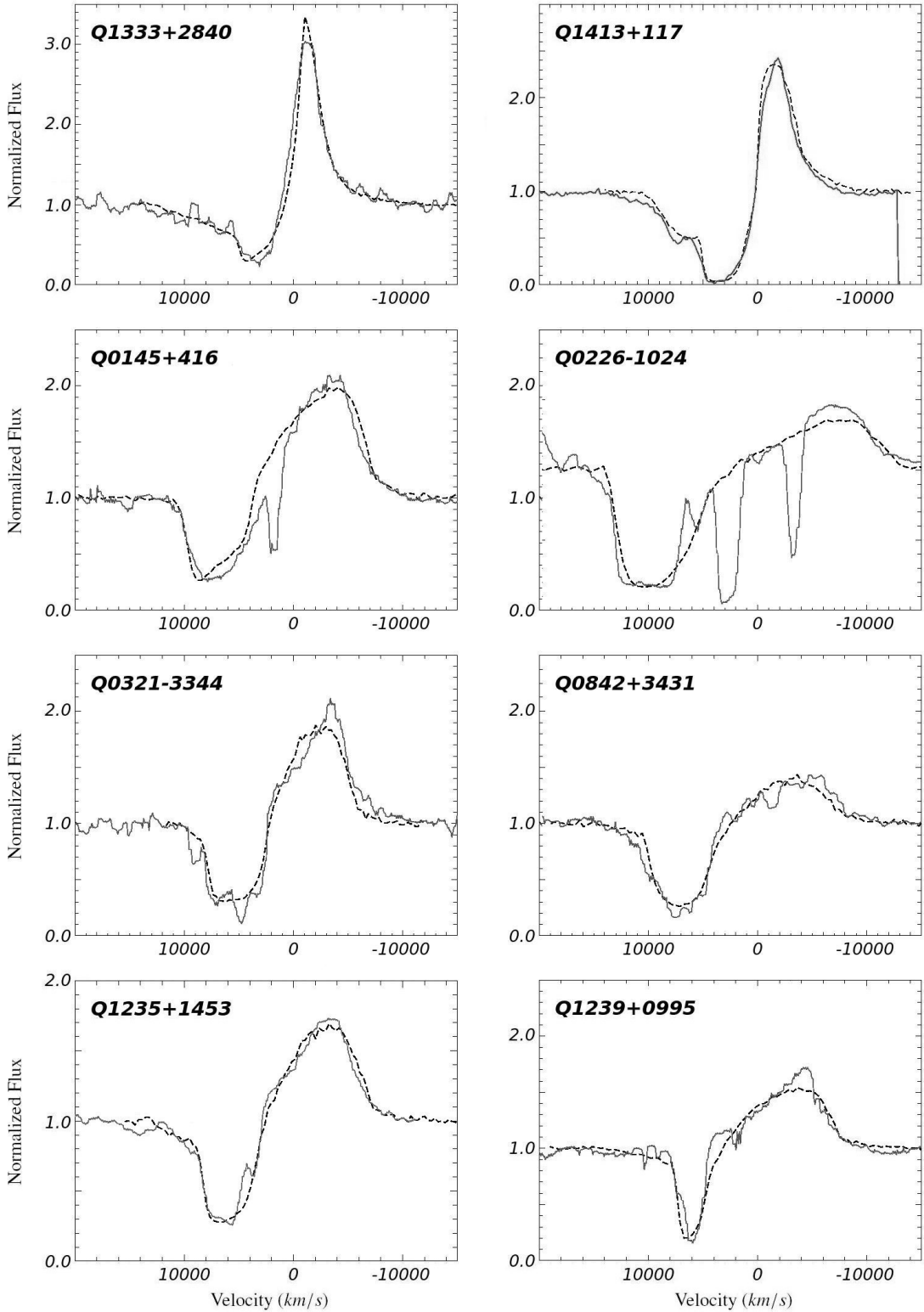


**Fig. 4.** Illustration of the best fit for eight out of the ten C IV line profile selected from the BAL quasar sample of Korista et al. (1993). The observed spectrum is represented by a full line and the two-component model profile by a dashed line. We note a good qualitative agreement between the observed line profile and the model. Each spectrum is normalized to the continuum level and represented as a function of the velocity.

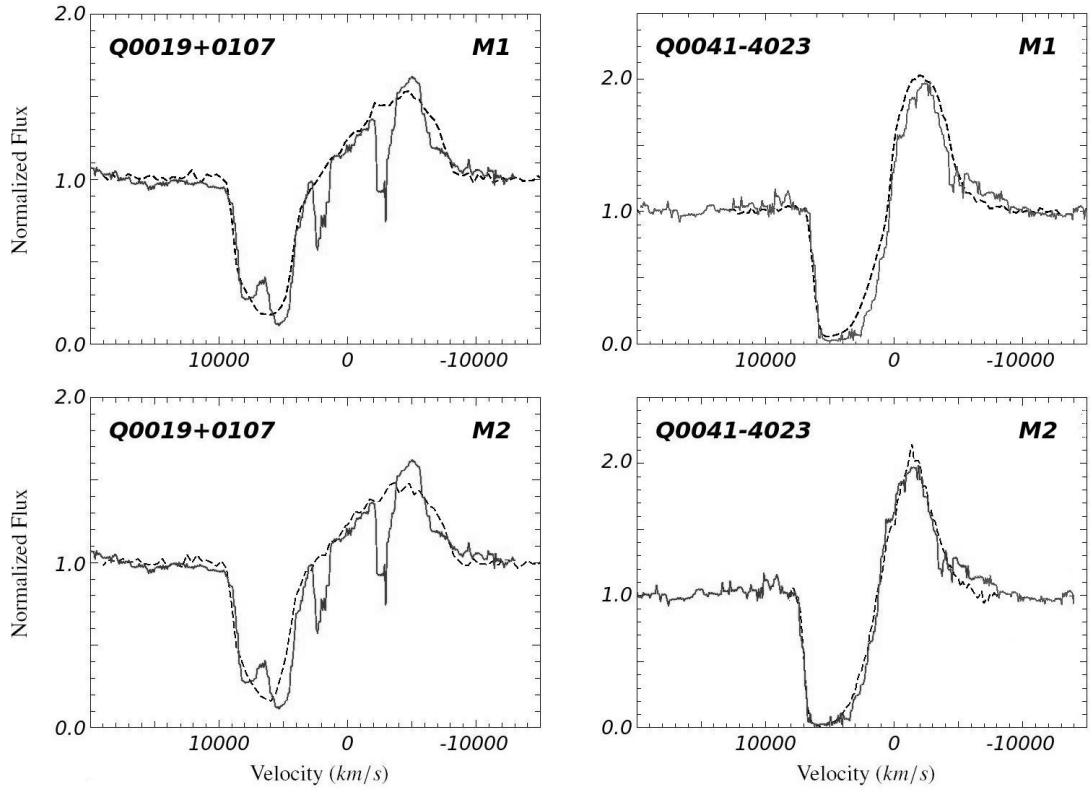


**Fig. 5.** Illustration of the non-uniqueness of the fit for two particular objects of our sample. The upper panels (labelled M1) of this figure show that the C IV line profile of these two objects can be fitted in the framework of the two-component wind model. In the lower panels (labelled M2), we show that the lack of typical two-component wind signatures in the line profile allows alternative fits with different parameters (see text). As in Fig. 4 the observed spectrum is represented by a full line and the two-component model profile by a dashed. Each spectrum is normalized to the continuum level and represented on a velocity scale.